Journal of Materials Processing Technology 211 (2011) 1102–1111

Contents lists available at ScienceDirect

Journal of Materials Processing Technology

journal homepage: www.elsevier.com/locate/jmatprotec

Numerical and experimental study of thermally induced residual stress in the hybrid laser–GMA welding process

Fanrong Kong, Junjie Ma, Radovan Kovacevic*

Research Center for Advanced Manufacturing, Southern Methodist University, 3101 Dyer Street, Dallas, TX 75205, USA

ARTICLE INFO

Article history:
Received 1 November 2010
Received in revised form 6 January 2011
Accepted 12 January 2011
Available online 18 January 2011

Keywords:
Laser welding
Gas metal arc welding (GMAW)
Hybrid laser–GMA welding
Finite element model (FEM)
Residual stress

ABSTRACT

A model based on a double-ellipsoidal volume heat source to simulate the gas metal arc welding (GMAW) heat input and a cylindrical volume heat source to simulate the laser beam heat input was developed to predict the temperature field and thermally induced residual stress in the hybrid laser–gas metal arc (GMA) welding process. Numerical simulation shows that higher residual stress is distributed in the weld bead and surrounding heat-affected zone (HAZ). Effects of the welding speed on the isotherms and residual stress of the welded joint are also studied. It is found that an increase in welding speed can reduce the residual stress concentration in the as-weld specimen. A series of experiments has been performed to verify the developed thermo-mechanical finite element model (FEM), and a qualitative agreement of residual stress distribution and weld geometrical size is shown to exist.

1. Introduction

The increased interest by industry and academia for hybrid laser/arc welding is because this technique has shown high efficiency and a reduction in production cost compared to separate laser welding or arc welding techniques. The hybrid laser–arc welding process is finding application in heavy industry, automotive, pressure vessels, etc. for welding thick steel plates, difficult-to-weld materials such as aluminum and magnesium, and welding dissimilar materials such as welding aluminum to steel and magnesium. A general overview of hybrid laser–arc welding and its applications was presented by Peyffarth and Krivt (2002).

The arc welding heat source is gas metal arc welding (GMAW) or gas tungsten arc welding (GTAW). GMAW can improve the chemical composition of a base metal by choosing the corresponding filler material. Laser welding combined with GMAW is characterized by wider and deeper welds, lower heat input that manifests lower distortion, good gap bridge ability, lower usage of laser power with respect to autogenous laser welding, higher welding speed, and improved weld quality.

Previous studies on the laser–gas metal arc (GMA) hybrid welding process are focused mainly on experimental optimization of processing parameters for a selected material with different joint configurations, monitoring and control of the welding process, and metallurgical analysis of the weld. Wang et al. (2008a) experimentally studied the effect of welding parameters on weld penetration in the hybrid laser–metal inert gas (MIG) welding of an aluminum alloy. Wang et al. (2008b) investigated the effects of setup conditions of a laser head and arc torch and the laser beam parameters on wire melting phenomena and gap tolerance in the hybrid laser–MIG arc welding of an aluminum alloy. Hayashi et al. (2003) studied the effect of gap tolerance on the weld quality of a high power CO_2 laser–MIG hybrid welding process. The behavior of laser-induced and arc plasmas near the molten pool during hybrid welding was observed with a black-and-white charge-coupled device (CCD) camera. Yao et al. (2006) experimentally studied the influence of joint geometry and fit-up gaps on hybrid laser–metal active gas (MAG) welding. Song et al. (2006) experimentally studied the overlap welding of magnesium alloy sheets by using the laser–arc hybrid process. Moore et al. (2004) studied the microstructures and properties of laser/arc hybrid weld and autogenous laser weld in pipeline steels. Gao et al. (2006) carried out a series of CO_2 laser–gas metal arc (GMA) hybrid welding experiments to study the effects of laser power, arc current, and the stand-off distance between laser and arc on the melting energy of CO_2 laser–GMA hybrid welding. Kim et al. (2006) observed the hybrid laser–MIG welding phenomenon in butt joints with different gap conditions by using a high speed camera. Qin et al. (2007) experimentally investigated the effects of Nd:YAG laser and pulsed MAG arc hybrid welding parameters on the weld shape. The obtained results indicated that the laser energy would affect the weld penetration and the weld width would depend on the arc parameters for a given welding speed.

Welding induced residual stress is one of the most critical factors affecting the final weld quality and lifetime of the welded

* Corresponding author.
E-mail address: kovacevi@lyle.smu.edu (R. Kovacevic).

0924-0136/$ – see front matter © 2011 Elsevier B.V. All rights reserved.
doi:10.1016/j.jmatprotec.2011.01.012

structure in real situations. To minimize and eliminate the negative effect of the welding process on the quality of the functional component or structure, an extensive research on welding distortions and residual stress has been performed by industrial and academic researchers. Studies based on experimental, analytical, and computational modeling methods are performed to study the evolution of residual stress in the welded structures for various applications. Hu and Richardson (2006) experimentally investigated the laser welding of high strength aluminum alloys. A large number of transverse cracks were found in the weld fusion zone. As one of the possible recommendations to mitigate the cracking problem, an additional heat source was used to alter the temperature distribution and, thus, reduce the cracking tendency.

Generally speaking, experimental trials take a long time and require a high cost to capture the optimal welding parameters. Numerical simulation is a cost-efficient way to help quantify the reasonable welding parameters and to further understand the mechanisms involved in welding. Current numerical studies on the welding process concentrate on traditional electric arc welding including GTAW, GMAW, and partly on laser welding (LW). These studies center on the heat transfer, fluid flow and solute diffusion in the weld pool, thermal induced distortion and residual stress, and grain growth in the heat affected zone (HAZ) and fusion zone (FZ). Deng et al. (2003) developed an uncoupled thermal-mechanical three-dimensional (3D) finite element model (FEM) to investigate the residual stress and deformation in low carbon and medium carbon steels welded by the tungsten inert gas (TIG) arc welding process, in which the effects of volume change due to austenite–martensite transformation on residual stress and distortions were studied. The analysis of low carbon steel revealed that the residual stresses and thermal deformations did not seem to be affected by phase transformation during cooling. However, for medium carbon steel, the residual stress and thermal deformations were significantly affected by the low temperature phase transformation. Abid et al. (2005) applied two-dimensional (2D) and 3D finite element models to predict welding distortions and residual stress in a pipe-flange joint. The heat input was modeled by using the Goldak double ellipsoidal heat source model. Temperature dependent material properties were used and deposition of filler metal was obtained by the element birth and death feature. Because the heat source model was difficult to identify, the relevant physical mechanisms were not fully understood. A few numerical simulations on the hybrid laser–arc welding have been published. Yoon et al. (2007) presented a plasma-augmented laser welding technology for manufacturing small-diameter steel tubes, in which a plasma arc was added to the single-laser heat source to join the conventional V-grooved butt joint of thin stainless steel strips. A finite element (FE) thermal analysis was performed to study the heat transfer process, where the laser beam was simply modeled as a general surface heat flux. Chen et al. (2003) tried to analyze the heat transfer mechanism in the hybrid laser–TIG welding process, and presented an energy-reduction point-line heat source model to simulate the heat transfer and mechanism of energy interaction. Liang et al. (2009) numerically analyzed an overlap welding of magnesium alloy. According to the hybrid welding interaction principle, a new hybrid heat source model was developed with finite element analysis. Zhou and Tsai (2008, 2009) investigated the mixing and diffusion processes in hybrid spot laser–MIG keyhole welding by developing a mathematical model and associated numerical techniques. Few numerical and experimental works on the thermally induced residual stresses in the hybrid laser–GMA welding process have been seen in public reports. However, those issues are meaningful to study to mitigate the final residual stress in the weld bead obtained by laser–GMAW hybrid technique and to further understand the hybrid welding mechanisms in a 3D view.

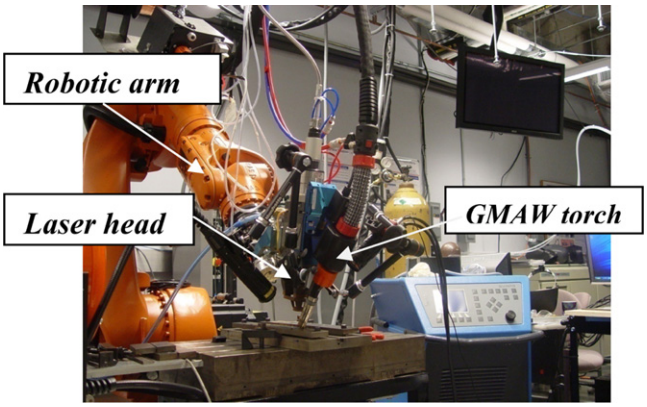

Fig. 1. Photo of hybrid laser–GMA welding system.

In this study, an experiment-based thermo-mechanical finite element model is developed to predict the temperature field and thermally induced residual stress in the hybrid laser–GMA welding process. A reasonable hybrid heat source model is presented to consider the specific heat input profiles due to the laser radiation and GMAW arc heating. Subsequently, an extensive experimentation is performed to validate the developed FEM.

2. Finite element modeling

2.1. Experimental process description

A continuous wave (CW) fiber laser with a power of 4 kW is used as a leading heat source, and a gas metal arc welding torch is following with a wire feedstock. A six-axis robot is used to control the welding path. The experimental setup is shown in Fig. 1. Laser power is set at 3.0 kW, GMAW arc current is set at 180 A, and arc voltage is set at 32 V. The sheet material is A36 mild steel, and the selected wire feedstock is ER70S-3 with a 1.0-mm diameter. The wire feed rate is kept constant at 11 mm/s. The coupons are clamped to the work table using the appropriate clamps. The schematic view of the clamping conditions and joint configuration is shown in Fig. 2. The configuration and dimensions of the butt joint are shown in Fig. 3a. A V-groove butt joint configuration is chosen (Fig. 3b). A shielding gas mixture, supplied through the GMAW torch, of 80% volume argon (Ar) and 20% volume carbon dioxide (CO_2) is used to protect the weld pool. After cooling down, the welded plate is cut by an abrasive water jet machine. The specimens are polished using standard metallographic procedures; then, the corresponding metallurgical microstructure at the cross-section of the specimens is checked by optical microscopy.

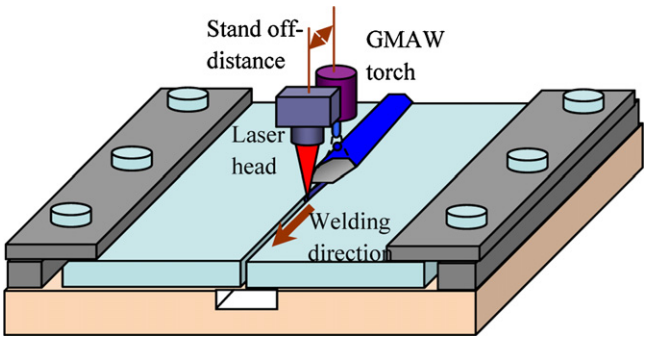

Fig. 2. Schematic of clamping condition and joint configuration.

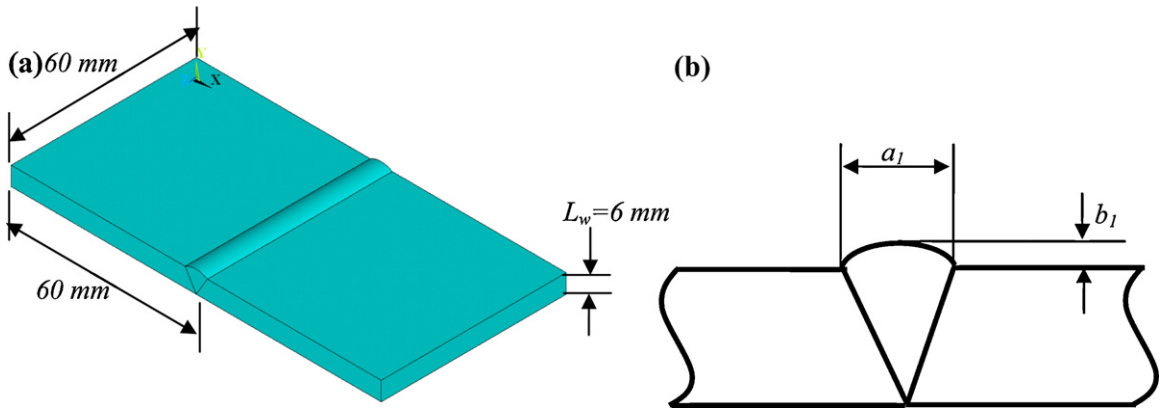

Fig. 3. (a) Schematic view of the joint configuration and (b) the close-up of groove segment.

Table 1
Temperature dependent thermal, physical and mechanical properties of ASTM A36 carbon steel.

Temperature (°C)	Specific heat (J/(kg°C))	Conductivity (W/(m°C))	Yield stress (MPa)	Thermal expansion coefficient ($\times 10^{-5}$/°C)	Young's modulus (GPa)
20	480	60	350	1.10	210
100	500	50	340	1.15	200
200	520	45	315	1.20	200
400	650	38	230	1.30	170
600	750	30	110	1.42	80
800	1000	25	30	1.45	35
1000	1200	26	25	1.45	20
1200	1400	28	20	1.45	15
1400	1600	37	18	1.45	10
1550	1700	37	15	1.45	10

2.2. Governing equations

2.2.1. Temperature field solution

Understanding the temperature field in the hybrid laser/arc welding process could be of importance in studying the outcomes of the welding process including full penetration, thermally induced cracking and stress, and phase transformation occurring in the HAZ. In the real welding situation, fluid flow induced heat convection is one of the important factors influencing the heat transfer in the weld pool zone. The convection term in this study is ignored in order to simplify the numerical solution. An alternate approach is applied, in which the thermal conductivity at a temperature higher than the melting point is revised by an incremental value, through which the heat transfer influence due to the convection in the weld pool is considered. The laser beam power is modeled as a volume heat source with a cylindrical Gaussian profile, and the GMAW arc power is assumed to be a double-ellipsoidal heat source (Fig. 4) (Goldak et al., 1984). Therefore, the governing equation of energy conservation is shown as follows:

$$\frac{\partial(\rho c T)}{\partial t} = \frac{\partial^2(k_m T)}{\partial x^2} + \frac{\partial^2(k_m T)}{\partial y^2} + \frac{\partial^2(k_m T)}{\partial z^2} + \dot{q}_{laser}(x, y, z, t) + \dot{q}_{arc}(x, y, z, t) \quad (1)$$

where t is the time, ρ is material density, c is the specific heat of material, and k_m is the thermal conductivity;

$$k_m = \begin{cases} k_0 & T < T_l \\ k_0 + k' & T \geq T_l \end{cases} \quad (2)$$

k_0 is the traditional thermal conductivity of the material used; k' is the additional value by which the convection heat transfer capability is equally considered in the proposed thermal modeling; T_l is the melting point of the material used; x, y, and z are Cartesian coordinates; and $\dot{q}_{laser}(x, y, z, t)$ is the laser radiation induced volume heat input and given by

$$\dot{q}_{laser}(x, y, z, t) = \eta_l \frac{P_{laser} \cos \Phi}{2\pi R_l^2} \times \exp\left(-\frac{(x - x_0)^2 + [z + (L_w - y)\tan \Phi - vt - D_{la}]^2 \cos^2 \Phi}{2R_l^2}\right) \cdot \frac{y}{L_w^2} \cdot \delta_l(x, y, z, t) \quad (3)$$

where v is the welding speed; η_l is the laser absorption efficiency by the welded material; P_{laser} is the nominal power of the laser beam; x_0 is the x-coordinate of the center point of the laser spot at the material surface; L_w is the thickness of the butt joint; R_l is the effective radius of the laser beam; Φ is the inclination angle of the laser head; D_{la} is the laser-to-arc stand-off distance. Φ is set at 0°; and D_{la} is set at 5 mm in this study. Considering that this proposed

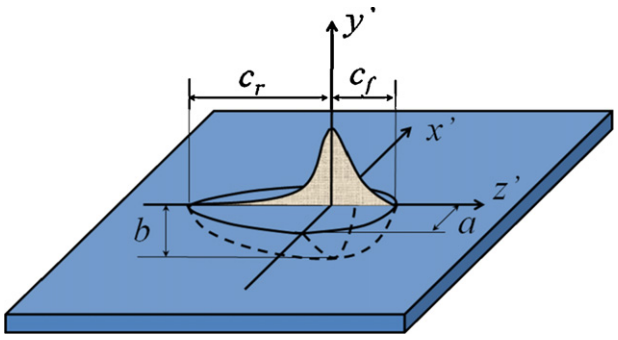

Fig. 4. Schematic of GMAW double-ellipsoid heat source model (Goldak et al., 1984).

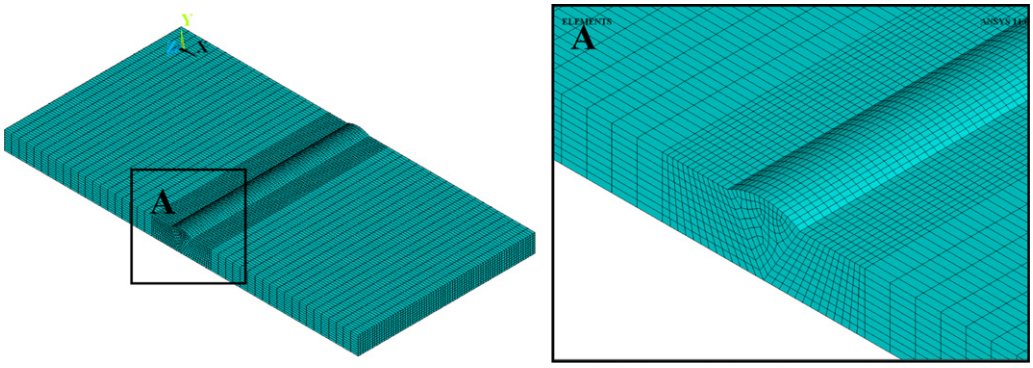

Fig. 5. Finite element mesh.

model is focused on the laser beam which precedes the GMAW arc torch with the stand off-distance between the laser beam and the center of feeding wire of 5 mm. This distance is larger than the sum of radius of laser beam (0.3 mm) and front effective radius of arc (c_f = 3 mm). Therefore, the influence of interaction between laser and arc on the energy distribution can be ignored due to the fact that these two heat sources are separated. $\delta_1(x, y, z, t)$ is the location control function defined as:

$$\delta_1(x,y,z,t) = \begin{cases} 1 & (x-x_0)^2 + [z + (L_w - y)\tan\Phi - vt - D_{la}]^2\cos^2\Phi \le R_l^2 \\ 0 & \text{otherwise} \end{cases} \quad (4)$$

The power densities of the double-ellipsoid heat source, q_{arc}^f (x, y, z, t) and q_{arc}^r (x, y, z, t), describing GMAW heat input distributions inside the front and rear quadrant of the heat source can be expressed as (Goldak et al., 1984):

$$\dot{q}_{arc}^f(x,y,z,t) = \frac{6\sqrt{3}f_f P_{arc}}{abc_f\pi\sqrt{\pi}} \exp\left(-\frac{3(x-x_0)^2}{a^2}\right) \cdot\exp\left(-\frac{3(y-L_w)^2}{b^2}\right) \cdot \exp\left(-\frac{3(z-vt)^2}{c_f^2}\right) \quad (5)$$

$$\dot{q}_{arc}^r(x,y,z,t) = \frac{6\sqrt{3}f_r P_{arc}}{abc_r\pi\sqrt{\pi}} \exp\left(-\frac{3(x-x_0)^2}{a^2}\right) \cdot\exp\left(-\frac{3(y-L_w)^2}{b^2}\right) \cdot \exp\left(-\frac{3(z-vt)^2}{c_r^2}\right) \quad (6)$$

where a, b, c_f, c_r are the characteristic parameters of heat sources. In this study, a, b, c_f, and c_r are set at 4 mm, 3 mm, 3 mm, and 7 mm, respectively. P_{arc} is the nominal power of the GMAW, and $P_{arc} = \mu UI$ where μ is the energy efficiency of GMAW by the welded material, U is arc voltage of GMAW, and I is the arc current of GMAW.

The boundary conditions at all the surfaces including heat losses from the convection and radiation are shown below:

$$-k(T)\frac{\partial T}{\partial n} = \sigma_0 \varepsilon(T^4 - T_\infty^4) + h_c(T - T_\infty) \quad (7)$$

where n is the normal outward vector to the surface of specimen, σ_0 is the Stefan–Boltzman constant, ε is emissivity, T_∞ is room temperature, and h_c is the surface heat transfer coefficient due to the convection of shielding gas.

Table 2
Characteristic geometrical sizes of weld bead measured by optical microscopy.

Welding speed (mm/s)	a_1 (mm)	b_1 (mm)
16	6.9156	0.7901
20	5.6745	0.5789
24	5.1540	0.4559

2.2.2. Stress–strain relationships

During the welding process, the total strain increment ($\Delta\varepsilon$) can be written as the sum of the individual components due to elastic ($\Delta\varepsilon^E$), plastic ($\Delta\varepsilon^P$) and thermal loading ($\Delta\varepsilon^T$), volumetric change, and transformation plasticity, respectively (Deng et al., 2003). In this study, a thermal-elastic–plastic model is used to study the thermally induced stress evolution and final residual stress in the hybrid laser–GTAW welding process in order to reasonably reduce the difficulty of convergence in the nonlinear thermo-mechanical FE analysis. Therefore, the strain increment can be written as follows:

$$\Delta\varepsilon = \Delta\varepsilon^E + \Delta\varepsilon^P + \Delta\varepsilon^T \quad (8)$$

2.3. Numerical procedure implementation based on ANSYS code

According to previous experience, it is usually difficult to acquire a convergent solution if a coupled thermo-mechanical FEM is directly applied on the welding process when the temperature-dependent material properties are used. This is because the

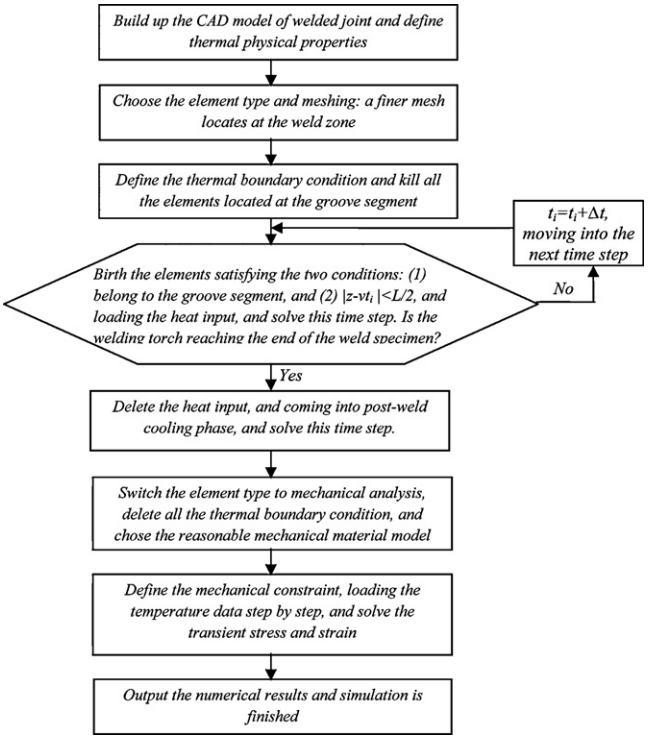

Fig. 6. Flowchart of numerical simulation procedure (where z is the centered coordinate of the element, v is the welding speed, t_i is the time, and L is the motion distance of welding head at each time step).

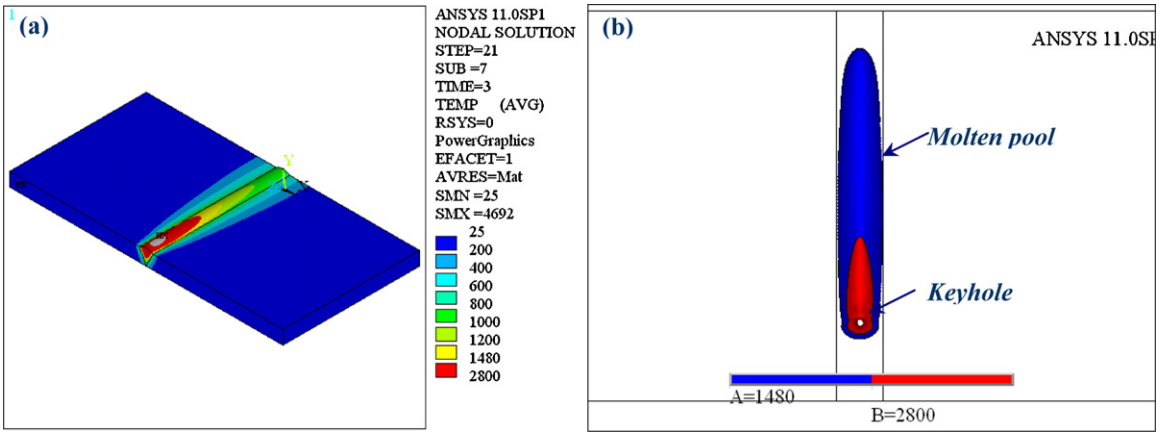

Fig. 7. Temperature distribution along the weld bead with the plate thickness of 6 mm: (a) general view of temperature and (b) characteristic isotherms of the molten pool and keyhole (welding speed is 16 mm/s).

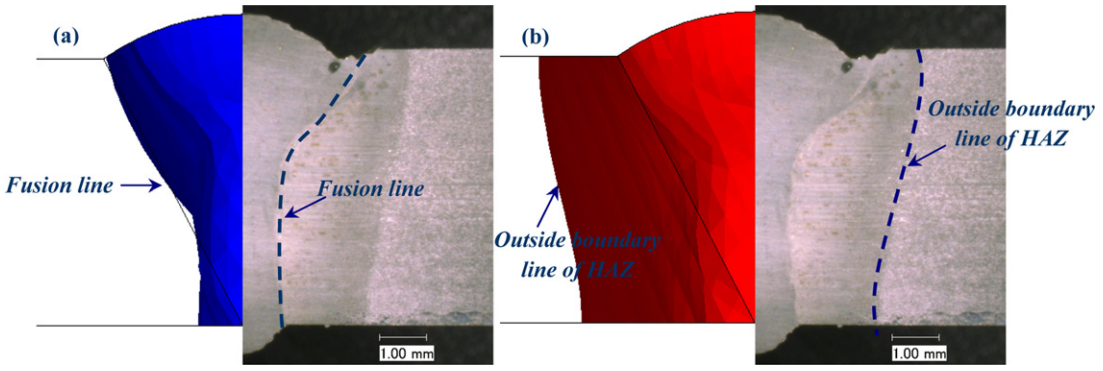

Fig. 8. Numerically predicted (left side) and experimentally obtained (right side) cross-sectional views of (a) fusion zone and (b) heat affected zone in the weld bead by hybrid laser–GMA welding (welding speed is 16 mm/s).

required sub-step numerical calculations to acquire a convergence solution in the thermal analysis are different from those in the mechanical analysis. Otherwise, a much larger sub-step number would need to be chosen to perform the thermal analysis and mechanical analysis simultaneously to reach the convergence state, and it would certainly be more computationally costly and could exceed the capability of a common personal computer. Therefore, an un-coupled thermo-mechanical FE analysis is performed in this study (Fig. 5). First, an FE thermal analysis is performed to acquire the whole temperature history during the welding and subsequent cooling processes. A non-uniform mesh is used, in which a finer mesh is located at the weld zone and HAZ in order to ensure enough numerical precision, and a coarse mesh is applied at the area far from the weld bead to reduce the whole computational cost. Subsequently, a mechanical analysis is implemented based on the same mesh configuration used in the thermal analysis. In ANSYS code, only the element type from the thermal field (SOLID70 is chosen in this study) is selected for the mechanical field (SOLID185 is correspondingly used), and to set the relevant mechanical properties of material. Then, the temperature history is applied as a thermal loading. At the same time, a mechanical constraint representing the real situation needs to be applied on the weld coupon. The whole numerical procedure is also shown in Fig. 6.

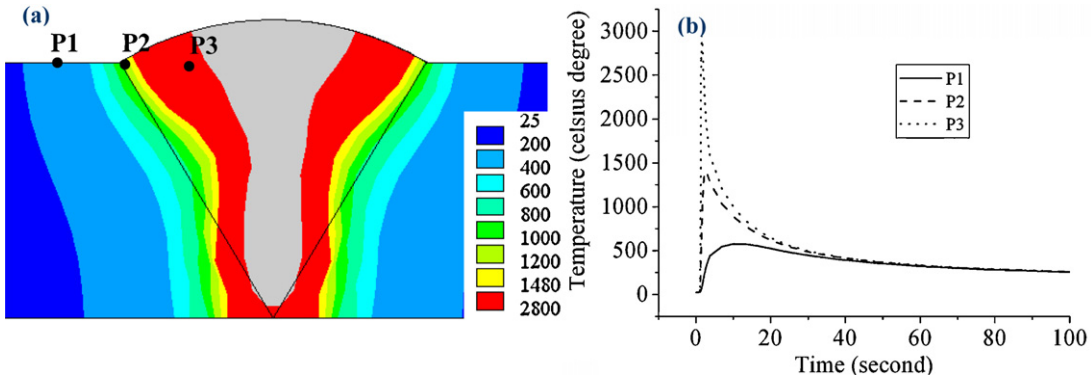

Fig. 9. Numerically predicted temperature distribution (a) across the weld (b) temperature evolution curve versus time at several positions marked in (a) (welding speed is 16 mm/s).

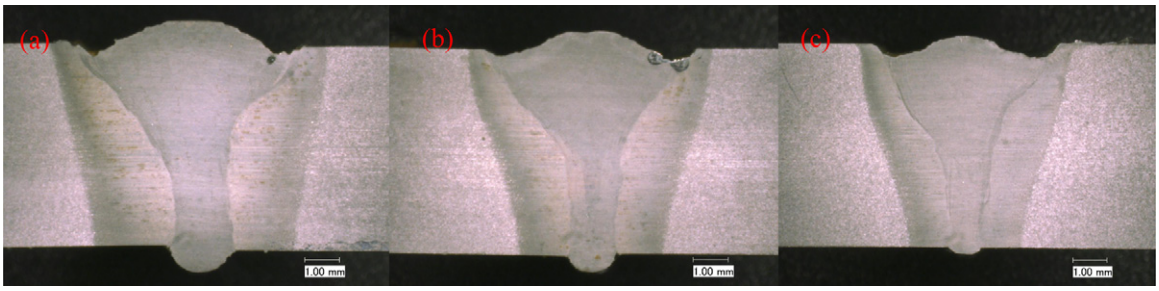

Fig. 10. Cross-sectional view of weld bead obtained by hybrid laser–GMA welding under three different welding speeds: (a) v = 16 mm/s, (b) v = 20 mm/s, and (c) v = 24 mm/s.

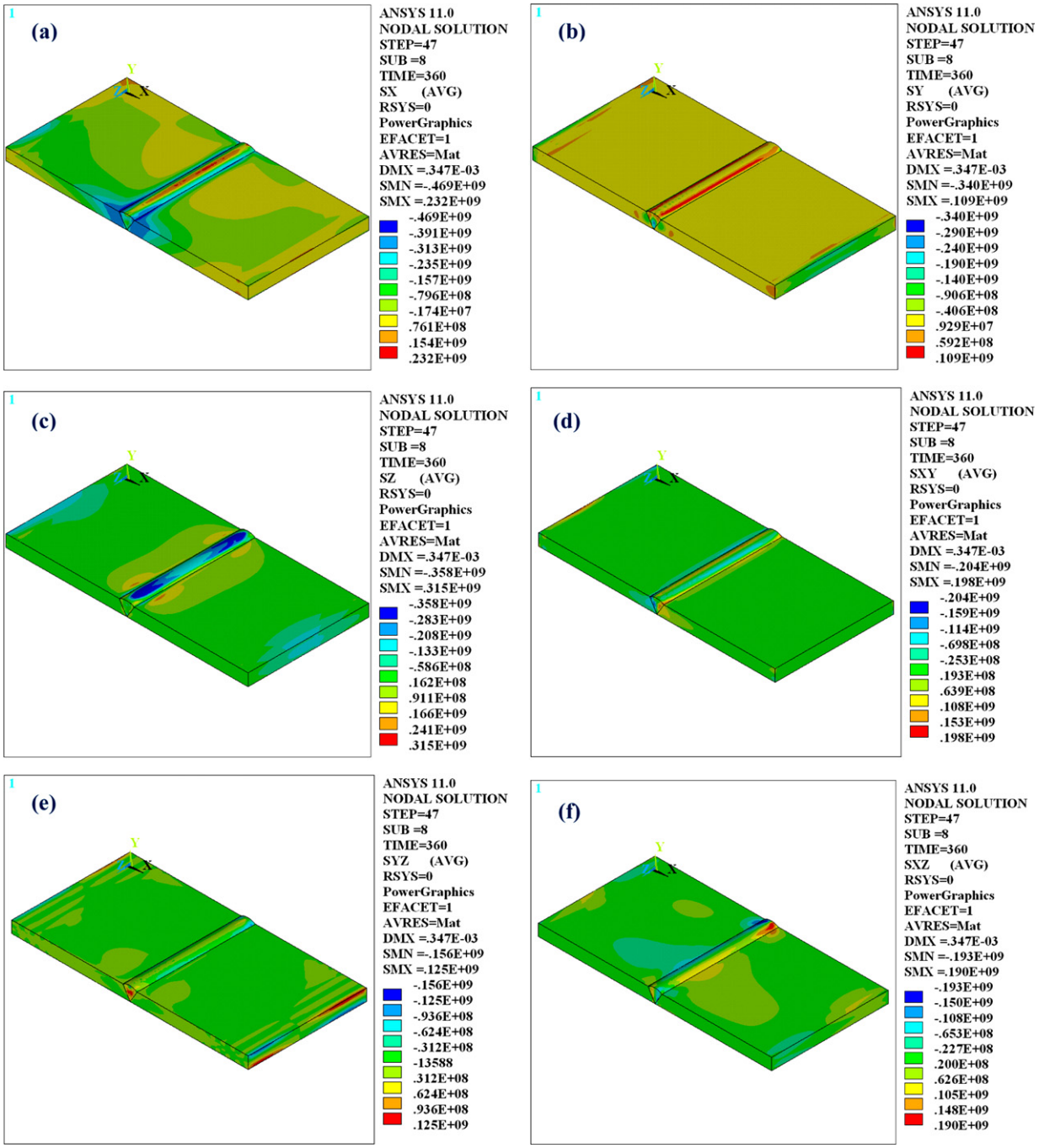

Fig. 11. Residual stress component contours of weld bead in the post-welded cooling phase: (a) transverse stress SX, (b) normal stress along the thickness SY, (c) longitudinal stress SZ, (d) x–y plane shear stress SXY, (e) y–z plane shear stress SYZ, and (f) z–x plane shear stress SZX (welding speed is 16 mm/s).

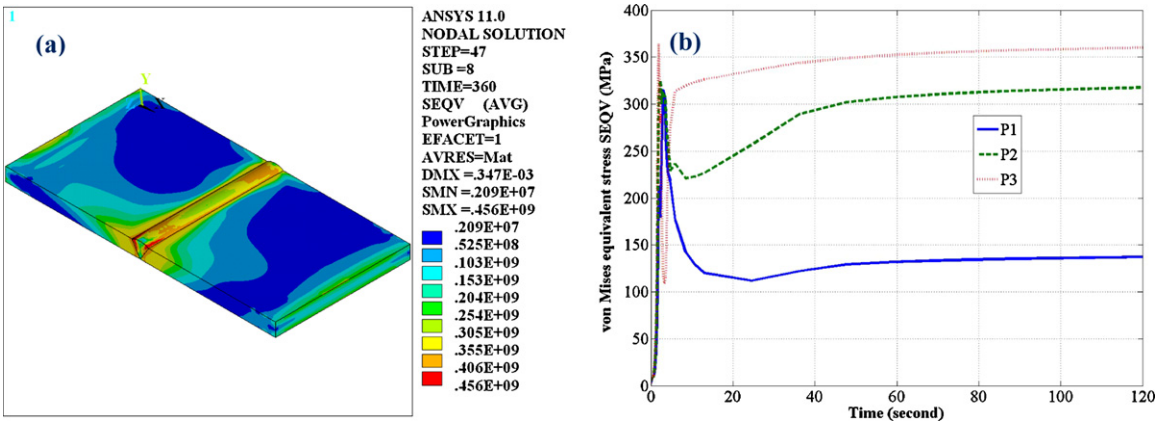

Fig. 12. (a) von Mises equivalent residual stress contour of weld bead at a welding speed of 16 mm/s, and (b) von Mises equivalent thermal stress evolution versus welding time at three characteristic locations on the top surface as shown in Fig. 9a.

For the simulation of the filling of the groove by a melted wire, a "death and birth" technique is used in the FEM. Initially, all the elements located at the groove are killed, and an empty groove is obtained. Subsequently, the elements located at the groove are activated segment by segment with time to simulate the weld bead formation by the filler material. The temperature-dependent material properties given in Table 1 are considered in the proposed model (Nadimi et al., 2008). In the simulation, the elastic stress-strain relationship of the welded material is assumed to obey the isotropic Hooke's law. The yielding behavior of the welded material satisfies the von Mises principle, and a bi-linear hardening principle is used to simulate the plastic behavior after the material is brought into the yielding state. The yielding stress of A36 is set at 350 MPa (at room temperature), and the corresponding tangential modulus is set at 2 GPa.

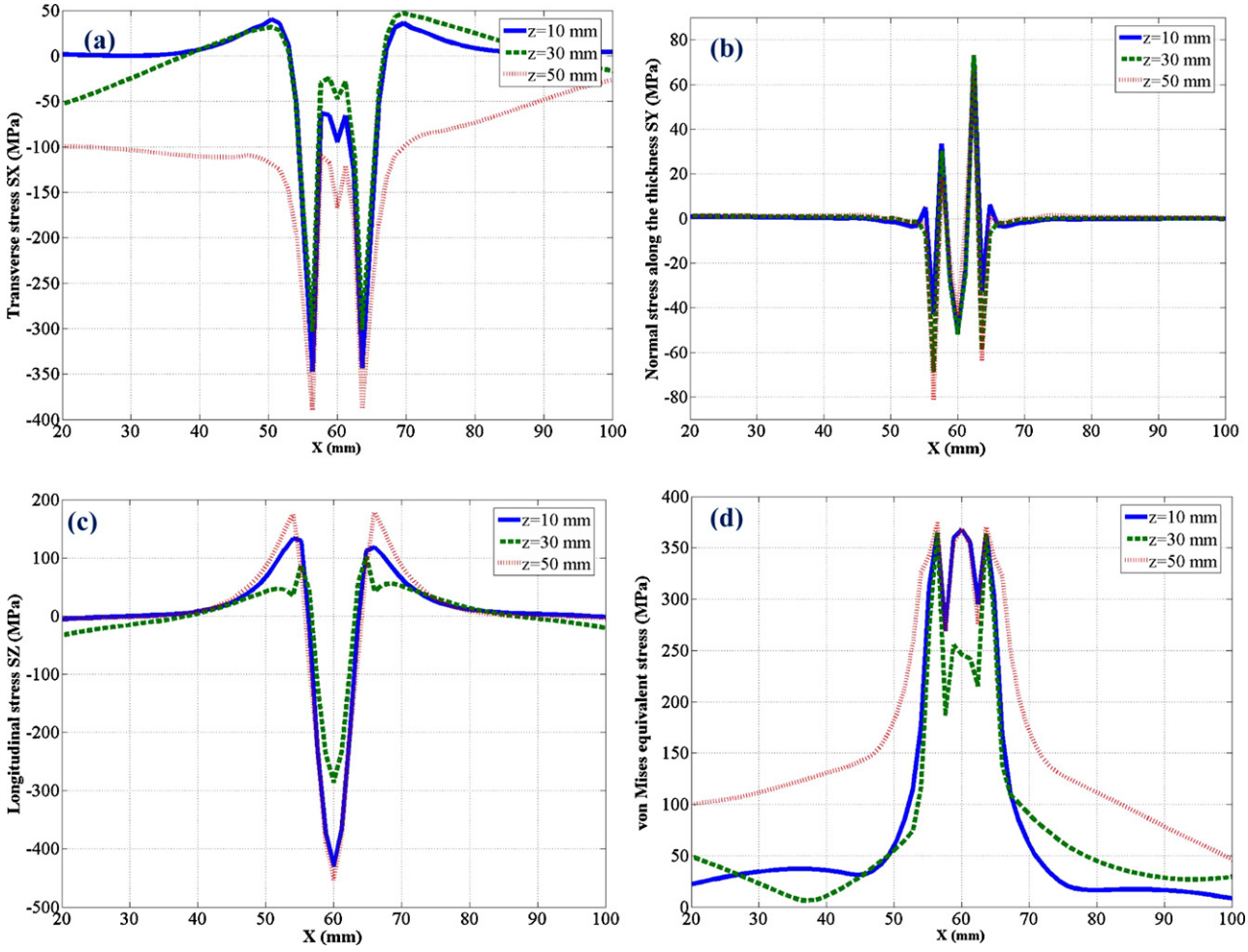

Fig. 13. Stress distribution transverse to the weld bead at three different paths of the top surface of weld bead obtained by hybrid laser–GMA welding: (a) transverse stress SX, (b) normal stress along the thickness SY, (c) longitudinal stress SZ, and (d) von Mises equivalent stress SEQV (welding speed is 16 mm/s).

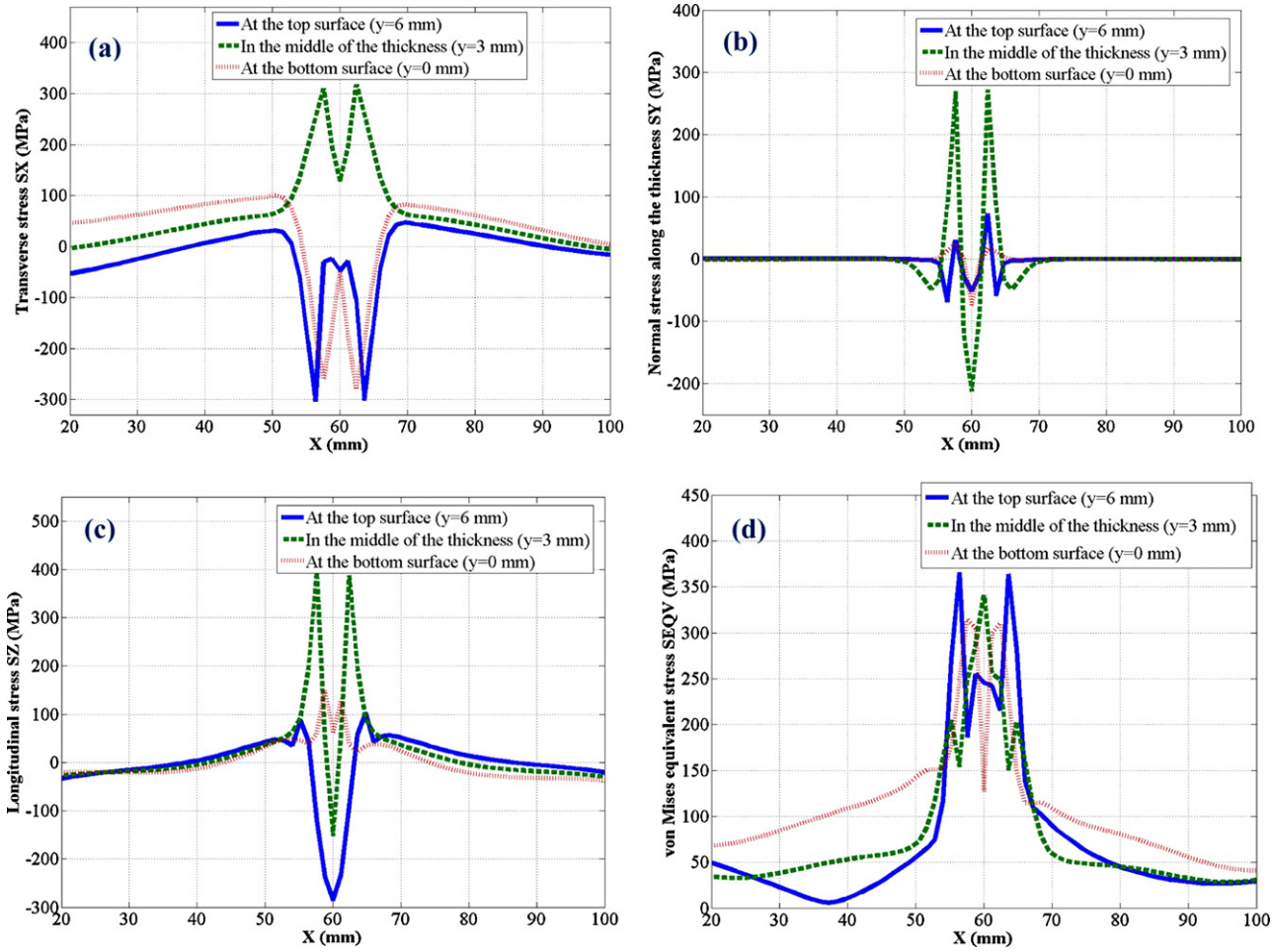

Fig. 14. Stress distribution transverse across the weld bead at the longitudinally middle section ($z = 30$ mm): (a) transverse stress SX, (b) normal stress along the thickness SY, (c) longitudinal stress SZ, and (d) equivalent stress SEQV (welding speed is 16 mm/s).

3. Results and discussion

In this study, a V-groove butt joint configuration is chosen (Fig. 3b), the characteristic geometrical sizes of weld bead are measured (Table 2), and they are used as the input into FE thermal model. Numerically predicted temperature distribution along the weld bead is shown in Fig. 7a, and characteristic isotherms of the molten pool and keyhole are shown in Fig. 7b. Laser beam radiating on the weld material produces a keyhole zone in the weld pool of a long tail profile. The boiling point of A36 steel is assumed to be 2800 °C. The numerical solution of FE thermal analysis of the hybrid laser–GMA welding process supplies the predictions of fusion zone (Fig. 8a) and the heat affected zone (HAZ) profiles (Fig. 8b), which are in a good agreement with experimentally obtained results. The cross-sectional view of the weld bead looks like a profile of a wine glass. The GMAW heat source has a wider heating radius than the laser heat source, which decides the final width of the hybrid weld. On the other hand, the laser has a primary role in deciding the final penetration depth of the hybrid weld. Fig. 9a shows a cross-sectional view of the weld bead with three points (P1–P3) at the distances from the center line for which the temperature evolution curves are numerically obtained as shown in Fig. 9b. The FE analysis shows that a high temperature gradient exists at the weld zone, where melting occurs by arc heating and laser radiation. For points farther from the weld center, the peak value of the temperature history is decreased. When the welding process is done, the welded specimen is cooled gradually to room temperature (Fig. 9b). Fig. 10 shows the cross-sectional views of the weld beads obtained by the hybrid laser–GMA welding technique under three different welding speeds of 16, 20, and 24 mm/s, respectively. It could be concluded that the full penetration is achieved in all three cases. However, narrower weld widths at both the top and bottom of the welds are obtained when a higher welding speed is applied, as shown in Fig. 10.

The results of the FE thermal analysis are applied as a load for the subsequent mechanical analysis of welding residual stress. Fig. 11a–c shows the contours of residual normal stress components of weld bead. Fig. 11d–f shows the contours of the residual shear stress components of the weld bead. It can be clearly found that a 3D residual stress state existed at the weld bead obtained by hybrid laser–GMA welding, and the magnitudes of the normal stress components are slightly higher than those of shear stress. In the case of the 16 mm/s welding speed, the peak value of residual transverse stress, 469 MPa (Fig. 11a), and longitudinal stress, 358 MPa (Fig. 11c), are exceedingly larger than the yield strength of the base metal of 350 MPa, which shows that serious residual stress is definitely present at a coupon level.

The corresponding von Mises equivalent stress distribution is also calculated in order to determine the final residual stress state, which is shown in Fig. 12a. The results show that a higher stress concentration is located at the weld zone and surrounding HAZ. The peak value of equivalent stress in this welding condition is 456 MPa, which indicates the welding induced plastic deformation is retained at the weld zone. In order to further understand the generation process of residual stress and strain, an evolution curve of von Mises equivalent stress versus welding time at three

Table 3
Parameters used in the residual stress measurement by the X-ray diffraction technique.

Material	Diffraction plane	Diffraction angle, 2θ	Incident beam	Collimator diameter	Exposure time	Maximum beta angle interval	Number of beta angles	Beta angle oscillation	Acquisition time
Fe-α	(2 1 1)	156°	Kα-Cr	0.5 mm	6.5 s	−20° to +20°	10	±3°	120 s

characteristic locations, which are marked in Fig. 9a, is numerically calculated and shown in Fig. 12b. It can be seen that stress at each location varies with the welding time, and a maximum stress value exceeding the yield strength of material is produced in the welding process, which causes plastic deformation to be retained in welded material, and as a result, residual stress and strain states remain in the cooling coupons.

The corresponding normal stress components as well as the equivalent stress distributions transverse to the weld bead at three paths on the top surface as shown in Fig. 13a–d. Generally, similar trends of stress distribution are kept at these three paths. The high compressive transverse stress (Fig. 13a) and longitudinal stress (Fig. 13c) are located around the weld zone. In addition, the stress states also change with the thickness across the same cross-section. Fig. 14a–c shows the normal stress distributions along the cross-section of weld bead (z = 30 mm) at different thicknesses, and an equivalent stress evaluation at the same cross-sections is shown in Fig. 14d. The three locations across the thickness of the weld bead are selected to study the residual stress state. One location is at the top surface of weld bead, the second one is in the middle of the bead, and the third one is at the bottom of the bead. There exists a gradual transition of stress distribution along the thickness of the weld. For transverse stress SX (Fig. 14a), the stress distribution at the top surface is similar to that at the bottom, and higher compressive stresses are both located at the weld zone. However, a higher tensile transverse stress is located at the weld zone along the path in the middle of the thickness of the weld bead. For normal stress along the thickness SY (Fig. 14b), the stress distribution at the middle of the thicknesses has a higher peak value as compared to the other two locations. For the longitudinal stress SZ (Fig. 14c), the highest peak value of compressive stress is located at the top surface of the weld zone, and the highest peak value of tensile stress is in the middle of the weld bead. For the von Mises equivalent stress, there is a small reduction in the maximum value of the stress at the bottom of the weld bead with respect to those values at the top surface of the weld bead (Fig. 14d).

In order to validate the accuracy of the numerically modeled residual stress in the hybrid weld, an X-ray diffraction technique is used to measure the residual stresses at the weld coupon's top surface by using the Laboratory Non-Destructive Residual Stress Measurement System (Proto Manufacturing Ltd., Canada). The diffraction parameters are presented in Table 3. The transverse stress (SX) and longitudinal stress (SZ) distributions along the characteristic path obtained by three different welding speeds of 16 mm/s, 20 mm/s, and 24 mm/s are shown in Fig. 15a and b, respectively. The weld coupon with measured path is shown in Fig. 15c. It is shown that a qualitative agreement exists between the experimentally obtained and numerically predicted residual stresses. The residual stress concentration tends to decrease with an increase in welding speed. The discrepancy between the experimental data and numerically predicted ones is mainly caused by the measuring error of the X-ray diffraction machine due to the irregular surface of weld.

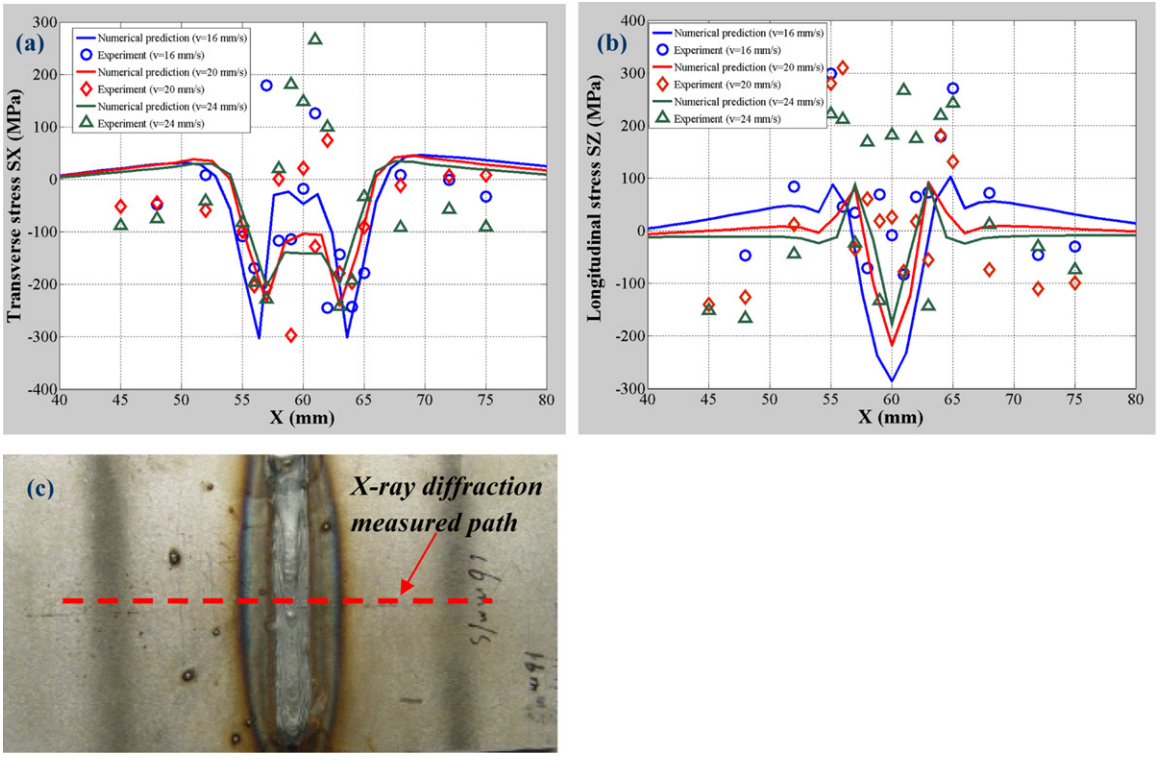

Fig. 15. Comparison of experimentally obtained and numerically predicted residual stress distribution across the weld bead at the top weld surface with three different welding speeds: (a) transverse stress SX, (b) longitudinal stress SZ, and (c) the schematic of numerically predicted and experimentally measured path at the top surface.

4. Conclusions

A 3D thermo-elastic–plastic FEM is developed to study the thermally induced residual stress in the hybrid laser–GMA welding process. Some important findings are achieved by the numerical simulation and experimental investigation shown below:

(1) 3D residual stress is present in the weld bead and adjacent HAZ, and higher compressive longitudinal and transverse stress is mainly present in the weld bead.
(2) The residual stress distributions obtained by the thermo-elastic–plastic FE analysis and X-ray diffraction measurement method are in a qualitative agreement.
(3) The effect of the welding speed on the heat distribution and residual stress along the weld joint is studied. A narrower bead width at both the top and bottom of the weld is achieved at a higher welding speed with a constant laser power and coupon size. However, an increase in welding speed can effectively reduce the residual stress concentration.
(4) The proposed thermo-mechanical FEM could be further applied to the optimization of the processing parameters of hybrid laser–GMA welding as well as other welding techniques.

Acknowledgements

The authors want to thank Dr. Shanglu Yang, currently a research engineer at General Motors China Science Lab, for his valuable help in the execution of experiments during his study at Southern Methodist University. This work was financially supported by NSF's Grant No. EEC-0541952.

References

Abid, M., Siddique, M., Mufti, R.A., 2005. Prediction of welding distortions and residual stresses in a pipe-flange joint using the finite element technique. Modelling and Simulation in Materials Science and Engineering 13, 455–470.
Chen, Y., Li, L., Fang, J., Feng, X., 2003. Numerical analysis of energy effect in laser–TIG hybrid welding. Journal of Materials Science and Technology 19, 23–26.
Deng, D., Luo, Y., Serizawa, H., Shibahara, M., Murakawa, H., 2003. Numerical simulation of residual stress and deformation considering phase transformation effect. Transactions of Joining and Welding Research Institute (Osaka University) 32 (2), 325–333.
Gao, M., Zeng, X.Y., Hu, Q.W., 2006. Effects of welding parameters on melting energy of CO_2 laser–GMA hybrid welding. Science and Technology of Welding and Joining 11 (5), 517–522.
Goldak, J., Chakravarti, A., Bibby, M., 1984. A new finite element model for welding heat source. Metallurgical Transactions B 15B, 299–305.
Hayashi, T., Kattayama, S., Abe, N., Ohmori, A., 2003. High power CO_2 laser–MIG hybrid welding process for increased gap tolerance—hybrid weldability of thick steel plates with square groove. Quarterly Journal of the Japan Welding Society 21 (4), 522–531.
Hu, B., Richardson, I.M., 2006. Mechanism and possible solution for transverse solidification cracking in laser welding of high strength aluminum alloys. Materials Science and Engineering A 429, 287–294.
Kim, Y.P., Alam, N., Bang, H.S., 2006. Observation of hybrid (cw Nd:YAG laser + MIG) welding phenomenon in AA 5083 butt joints with different gap condition. Science and Technology of Welding and Joining 11 (3), 295–307.
Liang, G.L., Zhou, G., Yuan, S.Q., 2009. Study on hybrid heat source overlap welding of magnesium alloy AZ31B. Materials Science and Engineering A 499 (1–2), 93–96.
Moore, P.L., Howse, D.S., Wallach, E.R., 2004. Microstructures and properties of laser/arc hybrid welds and autogenous laser weld in pipeline steels. Science and Technology of Welding and Joining 9 (4), 314–322.
Nadimi, S., Khoushehmehr, R.J., Rohani, B., Mostafapour, A., 2008. Investigation and analysis of weld induced residual stresses in two dissimilar pipes by finite element modeling. Journal of Applied Science 8, 1014–1020.
Peyffarth, P., Krivt, I.V., 2002. Laser–arc Processes and their Application in Welding and Material Treatment. Welding and Allied Processes, vol. I. Taylor & Francis, London.
Qin, G.L., Lei, Z., Lin, S.Y., 2007. Effects of Nd:YAG laser + pulsed MAG arc hybrid welding parameters on its weld shape. Science and Technology of Welding and Joining 12 (1), 79–86.
Song, G., Liu, L., Wang, P., 2006. Overlap welding of magnesium AZ31B sheets using laser–arc hybrid process. Materials Science and Engineering A 429, 312–319.
Wang, J., Nishimura, H., Fujii, K., Katayama, S., Mizutani, M., 2008b. Study of improvement of gap tolerance in laser–MIG arc hybrid welding of aluminum alloy. Journal of Light Metal Welding and Construction 46 (10), 11–22.
Wang, X., Wang, W., Lin, S., 2008a. Effect of welding parameter on weld penetration in laser–MIG hybrid welding of aluminum alloy. Transactions of the China Welding Institution 29 (6), 13–16.
Yao, Y., Wouters, M., Powell, J., 2006. Influence of joint geometry and fit-up gaps on hybrid laser–metal active gas (MAG) welding. Journal of Laser Application 18 (4), 283–288.
Yoon, S.H., Hwang, J.R., Na, S.J., 2007. A study on the plasma-augmented laser welding for small-diameter STS tubes. International Journal of Advanced Manufacturing Technology 32:, 1134–1143.
Zhou, J., Tsai, H.L., 2008. Modeling of transport phenomena in hybrid laser–MIG keyhole welding. International Journal of Heat and Mass Transfer 51, 4353–4366.
Zhou, J., Tsai, H.L., 2009. Investigation of mixing and diffusion processes in hybrid spot laser–MIG keyhole welding. Journal of Physics D: Applied Physics 42 (9), 095502.